3356–3365 *Nucleic Acids Research, 2020, Vol. 48, No. 6* *Published online 8 February 2020*
doi: 10.1093/nar/gkaa076

Structural basis of the zinc-induced cytoplasmic aggregation of the RNA-binding protein SFPQ

Jie Huang[1], Mitchell Ringuet[2], Andrew E. Whitten[3], Sofia Caria[1,4], Yee Wa Lim[1], Rahul Badhan[1], Victor Anggono[2] and Mihwa Lee[1,*]

[1]Department of Biochemistry and Genetics, La Trobe Institute for Molecular Science, La Trobe University, Melbourne, Victoria 3086, Australia, [2]Clem Jones Centre for Ageing Dementia Research, Queensland Brain Institute, The University of Queensland, Brisbane, Queensland 4072, Australia, [3]Australian Nuclear Science and Technology Organisation (ANSTO), Lucas Heights, NSW 2234, Australia and [4]SAXS/WAXS, Australian Synchrotron, ANSTO, Clayton, Victoria 3168, Australia

Received November 14, 2019; Revised January 23, 2020; Editorial Decision January 25, 2020; Accepted January 28, 2020

ABSTRACT

SFPQ is a ubiquitous nuclear RNA-binding protein implicated in many aspects of RNA biogenesis. Importantly, nuclear depletion and cytoplasmic accumulation of SFPQ has been linked to neuropathological conditions such as Alzheimer's disease (AD) and amyotrophic lateral sclerosis (ALS). Here, we describe a molecular mechanism by which SFPQ is mislocalized to the cytoplasm. We report an unexpected discovery of the infinite polymerization of SFPQ that is induced by zinc binding to the protein. The crystal structure of human SFPQ in complex with zinc at 1.94 Å resolution reveals intermolecular interactions between SFPQ molecules that are mediated by zinc. As anticipated from the crystal structure, the application of zinc to primary cortical neurons induced the cytoplasmic accumulation and aggregation of SFPQ. Mutagenesis of the three zinc-coordinating histidine residues resulted in a significant reduction in the zinc-binding affinity of SFPQ in solution and the zinc-induced cytoplasmic aggregation of SFPQ in cultured neurons. Taken together, we propose that dysregulation of zinc availability and/or localization in neuronal cells may represent a mechanism for the imbalance in the nucleocytoplasmic distribution of SFPQ, which is an emerging hallmark of neurodegenerative diseases including AD and ALS.

INTRODUCTION

The cytoplasmic aggregation of RNA-binding proteins (RBPs) through mutations and pathological conditions is an emerging hallmark of neurodegenerative diseases that include amyotrophic lateral sclerosis (ALS), frontotemporal lobar dementia (FTLD) and Alzheimer's disease (AD) (1,2). The most notable examples are trans-activation response element (TAR) DNA-binding protein 43 (TDP-43) and fused in sarcoma (FUS), which have been implicated in the onset and progression of ALS and FTLD, where imbalance in the nucleocytoplasmic distribution of these RBPs is observed. These RBPs are predominantly nuclear under normal conditions, however, they form cytoplasmic aggregates in the disease state. The RBPs implicated in neuropathological conditions often harbour low-complexity domains that are enriched with uncharged amino acids and are predicted to be intrinsically disordered. The majority of ALS- and FTLD-related mutations in the implicated RBPs are found within this region proposed to increase their propensity of the proteins to aggregate (1–3). Previous studies have probed the potential mechanisms of cytoplasmic aggregation of RBPs using transfected cell culture models. However, the molecular mechanisms that underlie pathological changes to endogenous proteins leading to RBP aggregation remain poorly understood.

Splicing factor proline- and glutamine-rich (SFPQ) is an abundant and ubiquitous RBP that plays roles in many aspects of RNA biogenesis including transcriptional initiation and termination, transcriptional activation and repression, and splicing (4,5). Along with two paralogues, non-POU domain-containing octamer-binding protein (NONO) and paraspeckle component 1 (PSPC1) from the *Drosophila* behavior human splicing (DBHS) protein family, SFPQ is found predominantly in the nucleus and has been implicated in a wide range of physiological functions including neuronal differentiation and development (5). It has been reported that SFPQ plays critical roles in neuronal differentiation during zebrafish brain development (6) and is required for neurotrophin-dependent axon survival through direct regulation of multiple mRNAs (7). In addition, loss of SFPQ specifically causes impaired transcriptional elongation, downregulating long genes in the developing mouse brain (8). Interestingly, an increas-

*To whom correspondence should be addressed. Tel: +61 3 9479 3248; Fax: +61 3 9479 1266; Email: mihwa.lee@latrobe.edu.au

ing body of evidence has also indicated abnormal cytoplasmic accumulation and loss of the nuclear pool of SFPQ in neuropathological conditions including AD, Pick's disease, FTLD, and ALS (9–11). Specifically, striking nuclear loss of SFPQ was demonstrated in the spinal cord tissue from sporadic ALS cases (11) and in the neurons of brain tissues from AD and Pick's disease patients (9). However, the molecular mechanisms triggering cytoplasmic mislocalization of nuclear SFPQ are still poorly understood.

The structure of SFPQ has been previously characterized, confirming the obligatory dimer formation that is characteristics of the DBHS protein family (12). More importantly, the crystal structure of SFPQ revealed a strikingly extended structure over 265 Å long formed by an unusual antiparallel coiled coil that results in an infinite linear polymer of SFPQ. Disruption of the coiled-coil mediated polymerization of SFPQ resulted in reduced nucleic acid binding *in vitro*, a reduced number of subnuclear bodies termed paraspeckles and a significant reduction in transcriptional activation, which could be rescued by the exogenous full-length SFPQ but not SFPQ variants that are incapable of polymerization (12). These findings collectively suggest that the polymerization of SFPQ is essential for the functions of SFPQ in transcriptional regulation and subnuclear body formation. Thus, any event affecting the ability of SFPQ to polymerize is a potential mechanism of misregulation, leading to aberrant gene regulation.

Here, we present zinc-induced polymerization of SFPQ that potentially competes with the functional polymerization mediated by the coiled coil. Based on the crystal structure of SFPQ in complex with zinc, we show that the application of zinc induces *in vitro* aggregation of SFPQ, and cytoplasmic aggregation and mislocalization of SFPQ in primary neuronal cells. These observations led us to propose dysregulation of zinc as a potential mechanism that causes an imbalance in the nucleocytoplasmic distribution of SFPQ in neurodegenerative diseases including AD and ALS. This study, to our best knowledge, is the first example providing the structural basis of the zinc-induced aggregation of an RBP implicated in neurological diseases.

MATERIALS AND METHODS

Plasmids for protein expression and purification

The construction of pCDF11-SFPQ-276-535 and pETDuet1-NONO-53-312 was described elsewhere (12,13). The following human SFPQ constructs were cloned into pGEX6p-1 (GE Healthcare) using the Gibson Assembly cloning method (New England Biolabs): SFPQ-276-535 (encoding amino acid residues 276–535), SFPQ-276-598 (encoding amino acid residues 276–598), and SFPQ-276-598 quadruple mutant (QM) (L535A, L539A, L546A, M549A) using the previously reported pCDF11-SFPQ constructs (12) as template for insert amplification. pGEX6p-SFPQ-276-535 triple mutant (TM) (H483A, H528A, H530A), pGEX6p-SFPQ-276-598 TM and pGEX6P-SFPQ-276-598 QM-TM were generated with the Q5 site-directed mutagenesis method (New England Biolabs) using oligonucleotides containing the base-pair substitutions. Human RXRα DNA-binding domain (DBD) (residues 130–228) was also cloned into pGEX6p-1 using the Gibson Assembly cloning method. All constructs were verified by DNA sequencing.

Protein expression and purification

Expression and purification of His_6-tagged SFPQ-276-535 was previously reported (12). Procedures of expression and purification of GST-tagged RXRα-DBD were adapted from the previous report (14). For expression of GST-tagged SFPQ constructs, pGEX6P-SFPQ constructs were transformed into *Escherichia coli* Rosetta2 (DE3) cells and recombinant proteins were produced by induction at an Abs_{600} of 0.6 with 0.5 mM isopropyl β-D-1-thiogalactopyranoside (IPTG) followed by incubation at 25°C overnight. Harvested cells were resuspended in lysis buffer [20 mM Tris–HCl (pH 7.5), 500 mM NaCl, 10% glycerol] and disrupted using a TS Series Benchtop cell-disruptor. The soluble fraction was incubated with glutathione sepharose 4B beads (GE Healthcare) at 4°C for 1 h. After washing with lysis buffer, the protein-loaded beads were incubated with GST-tagged human rhinovirus (HRV) 3C protease at a ratio of 1:50 (w/w) at 4°C overnight to cleave the GST-tag. The GST-tagged removed SFPQ constructs were subjected to size-exclusion chromatography using a HiLoad 16/600 Superdex 200 pg column (GE Healthcare) equilibrated with lysis buffer. For co-expression of SFPQ constructs with NONO-53-312, pETDuet1-NONO-53-312 was co-transformed with the appropriate pGEX6p-SFPQ constructs into Rosetta2 (DE3) and the SFPQ/NONO heterodimer purified as described above. All buffer solutions used in this study were pH titrated at room temperature.

Crystallization and X-ray diffraction data collection

Crystals of the Zn-SFPQ complex produced from the mixture of SFPQ-276-535 and RXRα-DBD-130-228 were grown by hanging-drop vapor diffusion method at 20°C. SFPQ-276-535 (2.5 mg/ml) and RXRα-DBD-130-228 (1 mg/ml), both in 20 mM Tris–HCl (pH 7.5), 500 mM NaCl were mixed at a molar ratio of 1:1 and incubated for 1 h before concentrated to 11.9 mg/ml. 2 μl of SFPQ-RXRα-DBD (11.9 mg/ml) was mixed with 2 μl of reservoir solution [0.1 M MES (pH 6.0), 0.2 M calcium chloride, and 14% (w/v) PEG 4000] and equilibrated against 0.5 ml reservoir solution. Plate-like crystals (150 × 50 × 10 μm) grew in two weeks. Diffraction data were recorded on beamline MX2 at the Australian Synchrotron (15) at a wavelength of 0.954 Å at 100 K. Additional datasets were collected for metal identification at low- and high-energy remote wavelengths, 9560 and 9760 eV, respectively, on beamline MX1 at the Australian Synchrotron at 100 K. Prior to cryocooling, crystals were successively transferred to artificial reservoir solutions containing 20% ethylene glycol in 10% increments. The data were processed with XDS (16), and merged and scaled with AIMLESS (17). Crystals belong to space group $P2_1$ with unit cell parameters of $a = 61.2$, $b = 62.5$, $c = 67.9$ Å and $\beta = 95.7°$. The asymmetric unit is estimated to contain one dimer of SFPQ, with a corresponding crystal volume per protein weight of 2.15 $Å^3$ Da^{-1} and a solvent content of 42.9%. Data collection and merging statistics for the native

Table 1. Diffraction data and refinement statistics[a]

Data collection	
Space group	$P2_1$
Unit cell parameters (Å, °)	61.2, 62.5, 67.9, $\beta = 95.7$
Resolution (Å)	27.38–1.94 (1.99–1.94)
No. of observations	154 554 (9,082)
No. of unique reflections	37 507 (2,239)
Completeness (%)	99.1 (89.6)
Redundancy	4.1 (4.1)
R_{merge} (%)	6.2 (60.0)
R_{pim} (%)	4.2 (40.1)
$CC_{1/2}$	0.998 (0.700)
Average $I/\sigma(I)$	10.3 (1.6)
Refinement	
R (%)	17.6 (20.2)
R_{free} (%)	21.8 (25.6)
No. (%) of reflections in test set	1999 (5.3)
No. of protein molecules per asu	2
R.m.s.d bond length (Å)	0.01
R.m.s.d bond angle (°)	1.03
Average B-factors (Å^2)[b]	35.4
Protein molecules	34.8
Zinc atom	22.6
Water molecules	42.0
Ramachandran plot[c]	
Residues other than Gly and Pro in:	
Most favored regions (%)	99.2
Additionally allowed regions (%)	0.8
Disallowed regions (%)	0
PDB code	6OWJ

[a]Values in parentheses are for the highest-resolution shell.
[b]Calculated by BAVERAGE in CCP4 Suite (19).
[c]Calculated using MolProbity (22).

data set are summarized in Table 1 and those for the data sets collected for metal identification in Supplementary Table S1.

Structure solution and refinement

The crystal structure was solved by molecular replacement using PHASER (18) within the CCP4 suite (19). The structure of the SFPQ homodimer (PDB code 4WII (12)) was used as search model after removing all non-protein atoms. The search model found a solution with a log likelihood gain (LLG) of 2,123 and a Z score of 22.9, locating one dimer in the asymmetric unit. Iterative model building with COOT (20) and refinement with autoBUSTER (21) was carried out. The final model consists of two chains of SFPQ (residues 284 – 535 in Chain A and residues 290–368, 371–535 in Chain B), one Zn atom, and 378 water molecules. The quality of the model was validated using MOLPROBITY (22). The refinement statistics are included in Table 1. The atomic coordinates have been deposited in the Protein Data Bank as entry 6OWJ.

Zinc-binding assay

The Zn-binding affinities of SFPQ protein constructs were determined using a competition assay between the proteins and the Zn(II)-saturated Fluozin-3 as previously described (23). Briefly, constant Fluozin-3 (150 nM) was titrated with a series of Zn(II) concentrations (0–600 nM) until the plateaued fluorescence signal was observed. The K_d(Zn(II)) was then determined by the following formula:

$$\frac{f - f_{min}}{f_{max} - f} = \frac{[Zn\,(II)]}{K_d}$$

where f_{max}, f and f_{min} represent the fluorescence signal of Fluozin-3 saturated with Zn(II), in the presence of Zn(II), and in the absence of Zn(II), respectively. K_d of Fluozin-3 to Zn(II) was calculated to 257 nM. All buffers were treated with Chelex® 100Resin (Bio-rad) to remove trace-metal contaminations prior to Zn-binding assay. Purified SFPQ constructs were incubated with ethylenediamine-tetraacetic acid (EDTA) at a molar ratio of 1:5 (protein: EDTA) at 4°C for 60 min before buffer exchange with the chelated buffer [20 mM MOPS (pH 7.0), 250 mM NaCl] using PD-10 desalting columns (Sigma-Aldrich). A series of Zn-binding assays were conducted with a range of protein concentrations (0–10 μM) of SFPQ constructs titrated to a constant FluoZin-3–Zn(II) concentration (150 nM) in 20 μl. Excitation-emission spectra readings were monitored by the decrease in fluorescence signal from the saturated Fluozin-3–Zn(II) complex using a CLARIOstar plate reader (BMG Labtech) with an excitation wavelength at 485 nm and emission wavelength at 520 nm at room temperature. The data were analysed by Prism (GraphPad Software) using the one-site non-linear fit with the K_d of Fluozin-3 to Zn(II) at 257 nM.

Small-angle X-ray scattering data collection and analysis

SAXS data for SFPQ-276-598 QM/NONO-53-312 and SFPQ-276-598 QM-TM /NONO-53-312, in 20 mM Tris–HCl (pH 7.5) and 250 mM NaCl, were collected on the SAXS-WAXS beamline at the Australian Synchrotron (24). Serial dilutions for each protein were prepared from a 3.0 mg/ml stock (yielding samples with concentrations of 3.0, 1.5, 0.75, 0.38 mg/ml) were loaded into a 96-well plate. Data reduction was carried out using Scatterbrain software (v 2.71) (http://www.synchrotron.org.au/aussyncbeamlines/saxswaxs/software-saxswaxs), and corrected for solvent scattering, sample transmission, and detector sensitivity. The estimated molecular mass was calculated using contrast and partial specific volumes determined from the protein sequences (25). Further data processing and Guinier analysis was performed using Primus (v 3.2) (26). The pair-distance distribution function ($p(r)$) was generated from the experimental data using *GNOM* (v 4.6) (27), from which $I(0)$, R_g and D_{max} were determined. Calculation of scattering profiles from atomistic structures was performed using CRYSOL (v 2.8.3) (28). Details of the data collection and processing can be found in Supplementary Table S2.

Plasmids for fluorescent protein fusions

pEGFP-SFPQ TM (H483A, H528A, H530A) was generated with the Q5 site-directed mutagenesis method (New England Biolabs) using oligonucleotides containing the base-pair substitutions and the wild-type pEGFP-SFPQ encoding full-length human SFPQ (12) as the PCR template. The incorporation of mutation was confirmed by DNA sequencing.

Zinc treatment and SFPQ localization assay

Primary cortical neurons were prepared from embryonic day 18 rat pups as described previously (29,30). Neurons were plated onto poly-L-lysine coated coverslips in Neurobasal growth medium supplemented with 2% B-27, 2 mM glutamax, 50 U/ml of penicillin, 50 μg/ml streptomycin and 5% fetal bovine serum (FBS). At days *in vitro* (DIV) 5, neurons were switched to 1% FBS Neurobasal medium and fed twice a week. To stop the growth of glial cells, 5 μM of uridine and 5-fluoro-2-deoxyuridine mixture were added once at DIV5. Transient transfection of cortical neurons was performed at DIV13 using Lipofectamine 2000 (Invitrogen) and used 16 h later. Transfected neurons were treated with 100 μM $ZnCl_2$ for 4 h, after which they were fixed with 4% paraformaldehyde/4% sucrose solution in PBS, washed and immediately mounted on glass slides using ProLong Diamond anti-fade mounting medium with DAPI (Invitrogen). Slides were imaged on a Zeiss Axio Imager slide scanner using the tile scan function and analyzed using Image J software (NIH). Fractions of neurons containing nuclear or cytoplasmic SFPQ aggregates over total transfected neurons were quantified and normalized to the group of GFP-SFPQ WT without $ZnCl_2$ treatment. MTT assay for cell viability test was performed using the CellTiter® 96 Non-Radioactive Cell Proliferation Assay Kit (Promega, G4000) according to the manufacturer's protocol. All animal handling procedures were carried out in accordance to the Australian code for the care and use of animals for scientific purposes by the National Health and Medical Research Council and were approved by the University of Queensland Animal Ethics Committee (AEC approval number QBI/047/18).

RESULTS

The crystal structure of SFPQ reveals unexpected zinc coordination by SFPQ

The structure of human SFPQ has been determined previously using different constructs: the dimerization domain (residues 276-535) (12,31) and the full-length DBHS domain with the intact coiled-coil domain (residues 276–598) (12) (Figure 1A). In this study, the same dimerization domain of SFPQ (referred as SFPQ-276-535 here in), encompassing two RNA-recognition motifs (RRMs), a NonA/paraspeckle (NOPS) domain and part of the coiled-coil domain, was crystallized in complex with Zn(II) (Figure 1B and Table 1). With no previous literature indicating zinc-binding activity of SFPQ, our finding of the Zn(II)–SFPQ complex was an unexpected, serendipitous discovery where the original crystallization was intended for co-crystallization of SFPQ with a nuclear hormone, RXRα, containing two zinc finger domains. Despite the presence of both proteins in the crystallization, the resulting crystals contained only SFPQ in complex with Zn(II).

The identity of the metal ion bound to SFPQ was unambiguously identified as Zn(II) by the calculation of anomalous difference Fourier maps from diffraction data collected at energies near the Zn(II) X-ray absorption edge: 9560 eV ($f'_{Zn} = 0.57$ e$^-$) and 9760 eV ($f'_{Zn} = 3.77$ e$^-$) (Supplementary Figure S1 and Supplementary Table S1). The overall structure of the Zn-SFPQ complex is consistent with the previously reported structures of the dimerization domain of SFPQ where extensive intermolecular interactions within the dimer primarily governed by hydrophobic interactions are observed (12,31). The main structural deviations are concentrated at the distal end of the truncated coiled-coil domain, which presents the zinc-binding site (Supplementary Figures S2 and S3).

In this structure, the Zn(II) coordination site lies between the two adjacent dimers (Figure 1C and D), with the metal coordinated by three histidine residues and a carbonyl oxygen: His A483, His B530, His A*528 and Leu A*535, where the asterisk (*) denotes a symmetry-related molecule (x, y, $z-1$) (Figure 1C and D). The residue His A483 is located in the C-terminal end of the NOPS domain while His A*528, His B530 and Leu A*535 reside at the distal end of the coiled-coil domain with Leu535 being the last residue of the truncated coiled-coil domain. This homotypic pattern of Zn(II) coordination by the two adjacent dimers continues with the following dimers, resulting in an infinite linear polymer of SFPQ-276-535 mediated by Zn(II) in the crystal (Figure 1E).

Our previous study revealed the coiled-coil mediated polymerization of SFPQ as critical for the cellular functions of SFPQ (12), while in this study, the crystal structure of SFPQ-276-535 reveals a different polymerization mechanism mediated by Zn(II). The Zn(II) coordination by SFPQ results in a significant conformational change in the α-helical secondary structure of the 'coiled-coil interaction motif', which is required for coiled-coil based polymerization (12) (Supplementary Figures S2 and S3), suggesting that Zn(II)-mediated polymerization can prevent the coiled-coil mediated polymerization that is critical for the physiological functions of SFPQ. In addition, the resulting Zn(II)-mediated polymerization of SFPQ decreases the intermolecular distance between the neighbouring dimers from 100 Å observed in the coiled-coil mediated polymerization (12) to 68 Å (Supplementary Figure S4).

SFPQ binds Zn(II) in solution

To test if the observed zinc-mediated polymerization of SFPQ in the crystal structure also occurs in solution, competitive zinc-binding assays were carried out by competition with the fluorescent Zn(II) indicator, Fluozin-3. In addition to the SFPQ construct (SFPQ-276-535) used in the crystallization study, the full-length DBHS domain with an intact coiled-coil domain (SFPQ-276-598) was assayed in order to determine the effect of truncation of the protein on its Zn(II)-binding affinity (Supplementary Figure S5). In addition, to verify that the measured zinc-binding affinities were due to Zn(II)-coordination by the three histidine residues (His483, His528 and His530) observed in the crystal structure, these histidine residues were mutated to alanine, to generate the variant protein SFPQ-TM (H483A/H528A/H530A).

The calculated Zn(II) affinities of SFPQ-276-535 wild-type (WT) and SFPQ-276-598-WT with the assumption of the stoichiometry of SFPQ dimer to Zn(II) being 1:1 were comparable: K_d of 0.28 and 0.23 μM, respectively (Figure 2 and Supplementary Table S3). The triple mutation of the

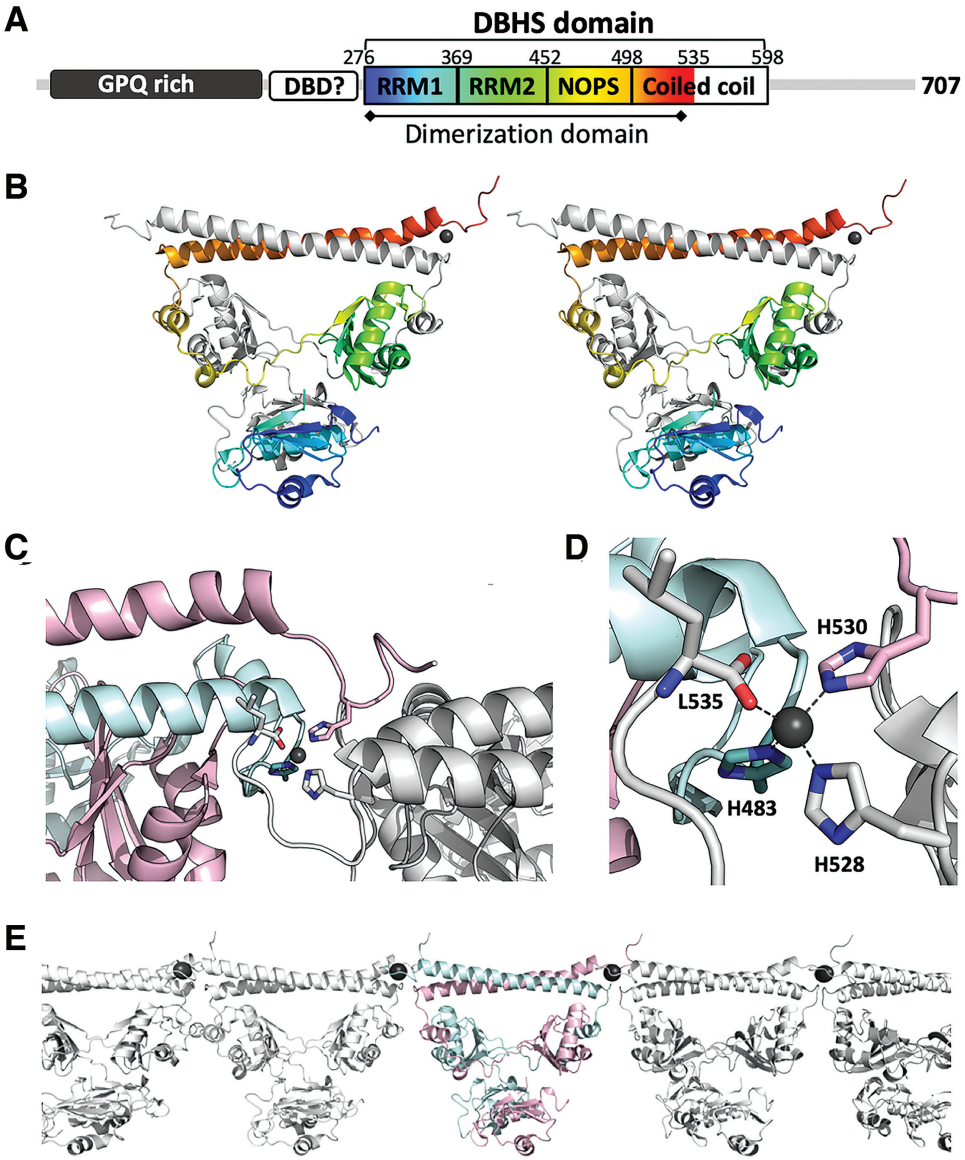

Figure 1. Crystal structure of the human SFPQ homodimer in complex with Zn(II). (**A**) Schematic domain organization of human SFPQ. Glycine, proline, glutamine (GPQ)-rich N-terminal region is followed by DNA-binding domain (DBD) of which precise boundary remains to be defined, and the DBHS domain composed of two tandem RNA-recognition motifs (RRM), NonA/paraspeckle (NOPS) domain and a C-terminal coiled coil. (**B**) Stereo view of the dimerization domain of human SFPQ in complex with Zn(II) in cartoon presentation with chain A in grey and chain B in the same color scheme as in (A). The Zn(II) atom is shown as black sphere. (**C**) Intermolecular interaction mediated by Zn(II). Chain A and chain B are shown in cyan and pink, respectively, while the neighboring dimer (symmetry operator, x, y, $z-1$) is shown in grey. (**D**) Close-up view of the Zn(II) center. (**E**) Zn(II)-mediated infinite polymerization observed in the crystal structure.

three Zn(II)-coordinating histidine residues caused a significant reduction in the affinity of SFPQ for Zn(II), evidenced by 31- and 26-fold increase in K_d: 8.24 μM for SFPQ-276-535-TM and 6.14 μM for SFPQ-276-598-TM, respectively (Figure 2 and Supplementary Table S3). This significant reduction of Zn(II)-binding affinities of SFPQ mutants indicates that the measured Zn(II)-affinities are due to specific interaction of the Zn(II)-coordinating residues of SFPQ and that the Zn(II)-binding site observed in the crystal structure is the same as that probed in solution in both constructs (truncated and full-length coiled-coil domain).

Zinc-induced polymerization of SFPQ occurs in solution

We also applied a small-angle X-ray scattering (SAXS) approach to confirm the Zn(II)-mediated polymerization of SFPQ in solution. As mentioned previously, SFPQ polymerizes in solution through its coiled-coil domain in a concentration-dependent manner (12). Therefore, we used the quadruple mutant SFPQ-276-598-QM (L535A/L539A/L546A/M549A) previously reported (12) to eliminate the polymerization effect mediated by the coiled-coil domain. In addition, the observation that heterodimerization of SFPQ with NONO is preferred to

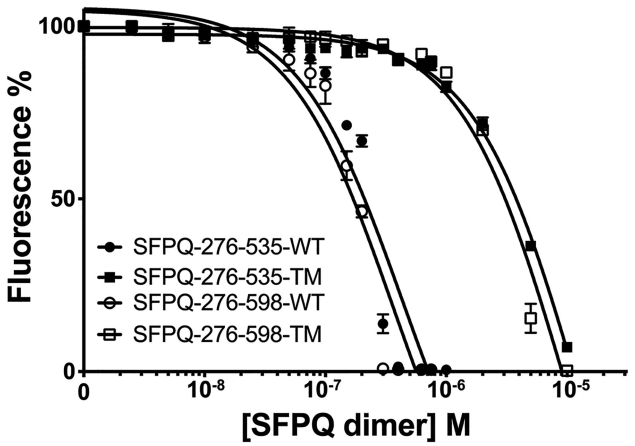

Figure 2. SFPQ binds Zn(II) in solution. The wild-type of two different constructs of SFPQ (SFPQ-276-535-WT and SFPQ-276-598-WT) showed sub-micromolar affinities for Zn(II) measured by a competition Zn(II)-binding assay using a Zn(II)-indicator, Fluozin-3, while mutations of the three histidine residues (TM) caused a significant decrease in Zn(II)-binding affinities. Data are presented with the standard deviation of three independent experiments ($n = 3$).

homodimerization and therefore, the SFPQ/NONO heterodimer may in fact more physiologically relevant than the SFPQ homodimer (32) led us to use the SFPQ-276-598-QM/NONO-53-312 heterodimer where SFPQ includes the full coiled-coil domain while the NONO construct includes only the dimerization domain (Supplementary Figure S5). SFPQ and NONO share 72% sequence identity within the DBHS domain (32). The two histidine residues corresponding to H528 and H530 in SFPQ are conserved in NONO while H438 in SFPQ is replaced by proline in NONO. However, the association with Zn(II) and formation of infinite linear polymer is still possible with the SFPQ/NONO heterodimer by adapting a rigid order of either an SFPQ/NONO-SFPQ/NONO or NONO/SFPQ-NONO/SFPQ configuration to utilize H483 from SFPQ. The triple mutation of the three Zn(II)-coordinating histidine residues to alanine (SFPQ-276-598-QM-TM/NONO-53-312) was again introduced to verify the effect of Zn(II) in the polymerization of SFPQ.

The resulting scattering data from SFPQ-276-598-QM/NONO-53-312 and SFPQ-276-598-QM-TM/NONO-53-312 were indistinguishable in the absence of Zn(II) (Figure 3A and C, Supplementary Figure S6 and Supplementary Table S2). The addition of 0.5 molar ratio of Zn(II) to the heterodimer, however, caused concentration-dependent protein association of SFPQ-276-598-QM/NONO-53-312, demonstrated by the upturn of the intensity profile at q-values below 0.05 $Å^{-1}$, clearly visible in the 1.5 mg/ml sample and amplified significantly in the 3.0 mg/ml sample (Figure 3B), while no apparent protein association was observed with SFPQ-276-598-QM-TM/NONO-53-312 in the presence of Zn(II) (Figure 3D). Therefore, the data demonstrate that the SFPQ/NONO heterodimer also undergoes Zn(II)-mediated polymerization in solution.

Application of zinc promotes cytoplasmic aggregation of SFPQ in primary cortical neurons

Based on the observations of *in vitro* Zn(II)-mediated polymerization of SFPQ in this study and the nuclear depletion and cytoplasmic accumulation of SFPQ observed in neurological diseases such as AD and ALS (9–11), we reasoned that altered zinc homeostasis leading to high zinc concentration in the neuropathological processes may cause the cytoplasmic aggregation of SFPQ. In fact, increased cytosolic zinc levels have been reported in the AD-affected cortex (33), in neurons derived from an AD transgenic mouse model (34) and in the spinal cords of transgenic mouse models of ALS and FTLD (35,36).

To facilitate this type of zinc dysregulation *ex vivo* and test our hypothesis that zinc dysregulation leading to high cytosolic zinc concentration may induce the cytoplasmic aggregation of SFPQ, we treated primary cortical neurons co-expressing a cell fill marker tdTomato and GFP-SFPQ (either wild-type or TM variant) with 100 μM $ZnCl_2$ for 4 h. Neurons were healthy and viable under this condition (Supplementary Figure S7). The concentration of $ZnCl_2$ administered was determined based on the previous study showing that overnight treatment of 50 μM $ZnCl_2$ resulted in a significant increase (72%) in the intracellular concentration of Zn(II) (37). In addition, it has been reported that neurons store up to 300 μM of free Zn^{2+} in nerve terminals and the estimates of synaptic Zn^{2+} release is in the range of 10–100 μM (38,39). In control neurons, GFP-SFPQ is primarily localized in the nucleus in the absence of added $ZnCl_2$ (Figure 4A). However, following $ZnCl_2$ treatment, there was a significant increase in the number of neurons with cytoplasmic GFP-SFPQ aggregates in the somatodendritic regions (Figure 4A and B, and Supplementary Figure S8). In contrast, zinc-induced aggregation was abolished in neurons expressing the GFP-SFPQ-TM variant protein (Figure 4A and B). Collectively, these data support the notion that high concentration of intracellular Zn(II) induces SFPQ aggregation and accumulation in the cytoplasm of primary neurons by promoting intermolecular interactions between SFPQ molecules (Figure 5).

DISCUSSION

SFPQ is a ubiquitous and multifunctional RBP, implicated in many aspects of RNA metabolism (4,5). More recent studies have shown the abnormal cytoplasmic accumulation and loss of nuclear pool of SFPQ in neuropathological conditions such as AD, ALS and FTLD (9–11). Although SFPQ is predominantly found in the nucleus, a non-nuclear pool of SFPQ has also been shown to be essential for axon motor development and viability (40). Collectively these data suggest that balance of the nucleocytoplasmic distribution of SFPQ is important for cellular homeostasis and responses to various stimuli.

In this study, we provide a molecular mechanism for the polymerization of SFPQ that is induced by Zn(II) binding to the protein, which results in an infinite linear polymer of SFPQ. To our best knowledge, this is the first study providing the structural basis of the zinc-induced aggre-

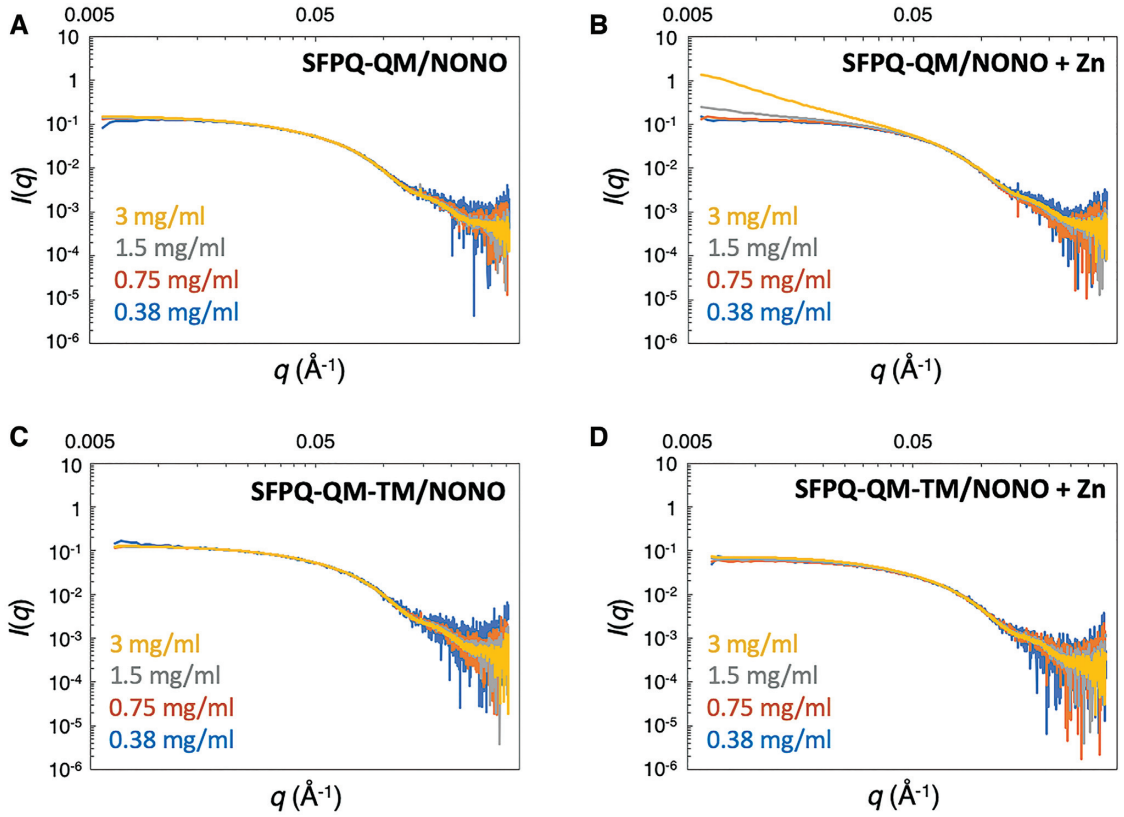

Figure 3. Zinc-induced aggregation probed by small-angle X-ray scattering. SAXS data were collected from: SFPQ-276-598-QM/NONO-53-312 in (**A**) the absence of Zn(II) and (**B**) the presence of Zn(II); SFPQ-276-598-QM-TM/NONO-53-312 in (**C**) the absence of Zn(II) and (**D**) the presence of Zn(II). The concentration series measurements have been scaled to the highest concentration sample so that the high-q portion of the data overlay and differences between the data sets can be clearly seen (0.38 mg/ml samples are shown in blue, 0.75 mg/ml samples in red, 1.5 mg/ml samples in grey, and 3.0 mg/ml samples in yellow). The Zn(II) concentration in (B) and (D) is fixed at an SFPQ/NONO heterodimer to Zn(II) ratio of 1:0.5).

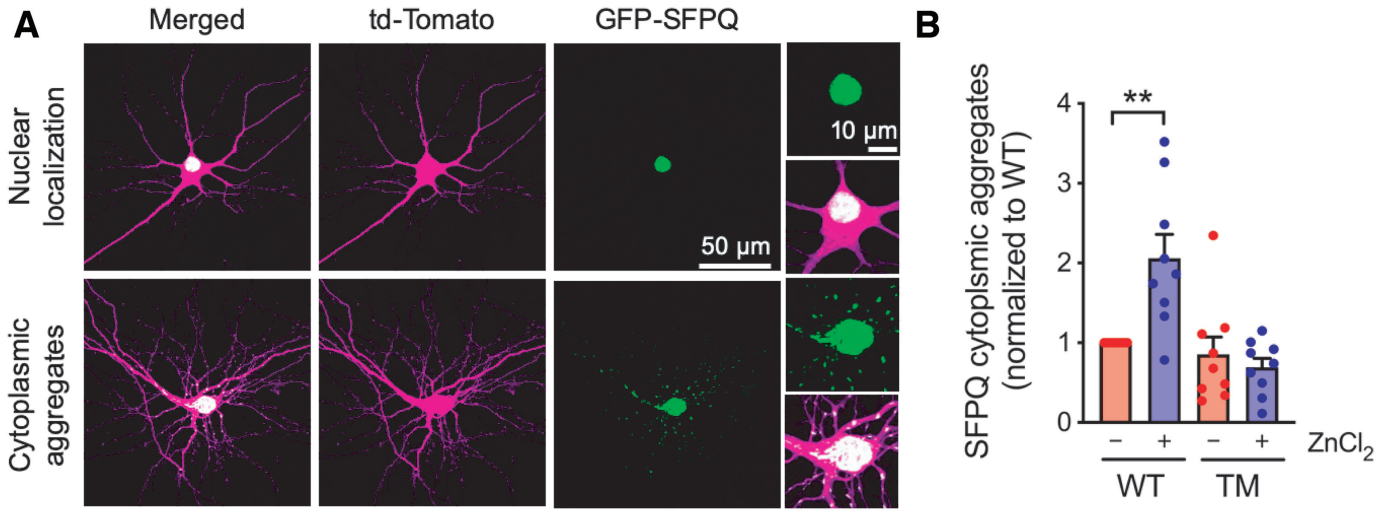

Figure 4. Zinc-induced cytoplasmic aggregation of SFPQ. (**A**) Representative confocal images of primary cortical neurons co-expressing a cell filled marker tdTomato (magenta) and GFP-SFPQ (green) exhibiting nuclear localization (top panel) or cytoplasmic aggregates in the somatodendritic regions (bottom). Higher-magnification images are shown on the right panels. (**B**) Quantification of the fraction of neurons with GFP-SFPQ cytoplasmic aggregates normalized to the value of control neurons. Over 1000 transfected neurons were examined per group ($n = 9$ coverslips from three independent experiments). Each dot on the bar graph represents the relative number of neurons containing GFP-SFPQ cytoplasmic aggregates normalized to GFP-SFPQ-WT-untreated group from one coverslip. Data represent mean ± SEM (one-way ANOVA, Tukey's post-hoc multiple comparison test, $^{**}P < 0.01$).

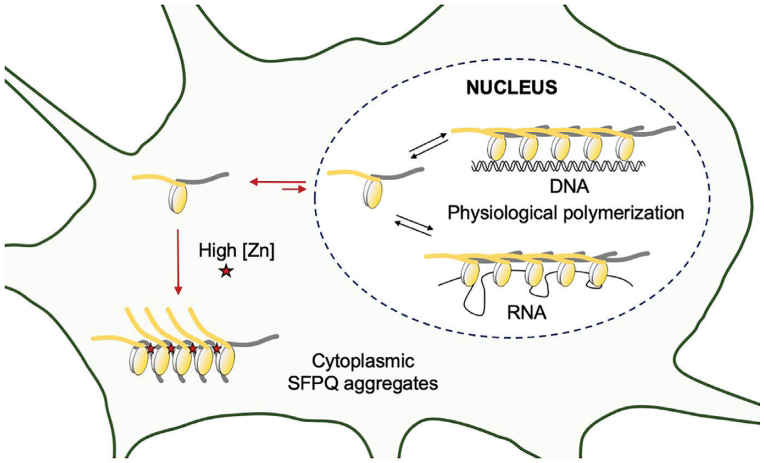

Figure 5. A proposed mechanism of the zinc-induced cytoplasmic aggregation of SFPQ in high Zn conditions. Under the normal physiological conditions, SFPQ polymerizes via the coiled-coil domain within the nucleus, which increases affinity and avidity to DNA and RNA interaction, while elevated levels of the intracellular zinc induce the zinc-induced polymerization of SFPQ, resulting in aggregation and accumulation of SFPQ in the cytoplasm.

gation of an RBP implicated in neurological diseases. The competitive Zn(II)-binding assay and SAXS data supported the observations made in the crystal structure that SFPQ undergoes Zn(II)-mediated polymerization in solution and that the three histidine residues His483, His528 and His530 which are conserved in SFPQ from most higher vertebrates (Supplementary Figure S9) are required for this polymerization. Furthermore, the treatment of cultured primary cortical neurons with a high concentration of Zn(II) induced aggregation and accumulation of SFPQ in the cytoplasm of these cells, mimicking the observations of SFPQ mislocalization that have been made in AD, ALS, and FTLD. Therefore, dysregulation of zinc leading to increased cytosolic zinc levels in neuronal cells may represent a potential mechanism that causes an imbalance in the nucleocytoplasmic distribution of SFPQ (Figure 5), which is an emerging hallmark of AD and ALS.

Altered metal homeostasis, in particular, dysregulation of zinc homeostasis – liberation of zinc in cytoplasm – in neurodegenerative disorders has been suggested to play a critical role in development of neuropathology (41–43). Under normal conditions, the majority of zinc in neurons is bound to zinc-binding proteins, thus, maintaining intracellular free zinc levels within the picomolar range while during neuronal injury and neuropathological conditions, zinc can be released from zinc-binding proteins due to oxidative stress and other unknown mechanisms (41–43). The association of amyloid-β (Aβ) with zinc has been implicated in the polymerization and aggregation of Aβ and the deposition of amyloid plaques in AD (38,39). The role of zinc in ALS and FTLD has been mainly established with Cu–Zn superoxide dismutase (SOD1) where mismetallation of this protein leads to protein misfolding and aggregation (44). However, recent studies have begun to unravel the association of zinc with TDP-43, which also induced the aggregation and cytoplasmic accumulation of this protein (37,45). Therefore, supported by our study presenting the structural basis of the zinc-induced polymerization of SFPQ, we suggest that SFPQ and other RBPs also undergo the metal-dependent aggregation, which results in mislocalization of these proteins from nucleus to cytoplasm when the cytosolic zinc concentration is increased in disease-affected neurons.

Our previous study has shown that the dynamic and functional polymerization of SFPQ mediated by the extended coiled-coil domain is critical for the cellular functions of SFPQ. The association of zinc with SFPQ results in a significant conformational change in the α-helical secondary structure of the extended coiled-coil domain, preventing the physiologically critical polymerization mode, which underpins the function of SFPQ in transcriptional regulation and subnuclear body formation in the nucleus. The two different modes of polymerization of SFPQ also resulted in different intermolecular distances: from 100 Å observed in the coiled coil mediated polymerization to 68 Å in the Zn(II)–SFPQ complex. Interestingly, it has been proposed that the extended coiled-coil domain functions as an elastic ruler, to position the core of the dimer at a specific distance along RNA interaction partners such as NEAT1 long non-coding RNA for subnuclear body, paraspeckle formation (46). Therefore, in addition to altering the nuclear and cytosolic distribution of SFPQ upon the increased cytosolic zinc concentration (Figure 5), the association of the nuclear pool of SFPQ with zinc will also likely have impact on the nucleic acid binding properties of SFPQ, and therefore its function in gene regulation and subnuclear body formation.

RBPs play multiple roles in many aspects of RNA metabolism for spatial and temporal control of gene expression in a wide range of biological contexts by forming extensive protein-RNA and protein-protein interactions in a large number of permutations. An increased demand of the RNA metabolism has been shown particularly in the brain through alternative mRNA processing such as alternative splicing, polyadenylation and targeted localization, and post-transcriptional silencing to diversify the strategies for gene expression in the brain cells (2). Therefore, it is not surprising that loss of nuclear population accompanied by cytoplasmic aggregation of RBPs is linked to neurological diseases. Although the two proteins use different domains for their polymerization (the N-terminal domain in TDP-43 versus the C-terminal coiled-coil domain in SFPQ), our

observations in this study are reminiscent of TDP-43, where functional and dynamic polymerization is essential for its function in the nucleus while cytoplasmic aggregation of TDP-43 is linked to the pathological condition in the majority of ALS (47).

It is unclear whether loss of the nuclear pool of SFPQ is a cause or merely an effect of the progression of neurodegenerative diseases. However, a recent report showed that loss of SFPQ caused impaired transcriptional elongation, resulting in the downregulation of long genes in the developing brain (8). Many of the downregulated long genes by SFPQ knockout are associated with neurodegenerative and psychiatric diseases, and essential for axon guidance, neuronal migration and synapse formation. These data indicate an essential role of SFPQ in gene expression during neuronal development. Another independent study also showed that loss of SFPQ caused altered Tau isoform ratio and induced FTLD-like behaviour in mouse (48). Based on these observations, it is likely that loss of the nuclear pool of SFPQ drives neuropathology by loss of its essential functions in the nucleus. Finally, whether the cytoplasmic aggregates of SFPQ are cytotoxic to the neurons – gain of function – similar to the debated cytotoxic role of TDP-43 aggregates in ALS (49) is an intriguing possibility.

In summary, our study provided the structural basis of the zinc-induced polymerization of SFPQ, an RBP linked to AD and ALS, offering a new framework how metal-induced polymerization of RBPs can induce cytoplasmic aggregation and accumulation of these proteins in neurodegenerative diseases. This framework may provide new diagnostic and/or therapeutic avenues for these diseases.

DATA AVAILABILITY

Atomic coordinates and structure factors for the reported crystal structures have been deposited with the Protein Data bank under accession number 6OWJ.

SUPPLEMENTARY DATA

Supplementary Data are available at NAR Online.

ACKNOWLEDGEMENTS

We thank A/Prof. Megan Maher for helpful discussion and Dr Saumya Udagedara for instruction for Zn(II)-binding assay (The University of Melbourne). Aspects of this research were undertaken on the Macromolecular Crystallography beamlines and SAXS-WAXS beamline at the Australian Synchrotron (Victoria, Australia), part of ANSTO, and made use of the Australian Cancer Research Foundation (ACRF) detector. We thank the beamline staff for their professional support. We acknowledge the La Trobe University-Comprehensive Proteomics Platform (La Trobe University) for providing infrastructure and expertise.

FUNDING

Australian Research Council Discovery Early Career Research Award (ARC DECRA) Fellowship [DE150101243]; Tracey Banivanua Mar Fellowship (La Trobe University, Melbourne, Australia to M.L.); Australian National Health and Medical Research Council Project Grant [GNT1138452]; Clem Jones Centre for Ageing Dementia Research (to V.A.); Imaging was performed at the Queensland Brain Institute's Advanced Microscopy Facility using a slide scanner microscope supported by the Australian Government through the Australian Research Council Linkage Infrastructure, Equipment and Facilities (ARC LIEF) grant [LE100100074]. Funding for open access charge: Tracey Banivanua Mar Fellowship, La Trobe University.
Conflict of interest statement. None declared.

REFERENCES

1. Nussbacher,J.K., Tabet,R., Yeo,G.W. and Lagier-Tourenne,C. (2019) Disruption of RNA metabolism in neurological diseases and emerging therapeutic interventions. *Neuron*, **102**, 294–320.
2. Conlon,E.G. and Manley,J.L. (2017) RNA-binding proteins in neurodegeneration: mechanisms in aggregate. *Genes Dev.*, **31**, 1509–1528.
3. Maziuk,B., Ballance,H.I. and Wolozin,B. (2017) Dysregulation of RNA binding protein aggregation in neurodegenerative disorders. *Front Mol. Neurosci.*, **10**, 89.
4. Yarosh,C.A., Iacona,J.R., Lutz,C.S. and Lynch,K.W. (2015) PSF: nuclear busy-body or nuclear facilitator? *Wiley Interdiscip. Rev. RNA*, **6**, 351–367.
5. Knott,G.J., Bond,C.S. and Fox,A.H. (2016) The DBHS proteins SFPQ, NONO and PSPC1: a multipurpose molecular scaffold. *Nucleic Acids Res.*, **44**, 3989–4004.
6. Lowery,L.A., Rubin,J. and Sive,H. (2007) Whitesnake/sfpq is required for cell survival and neuronal development in the zebrafish. *Dev. Dyn.*, **236**, 1347–1357.
7. Cosker,K.E., Fenstermacher,S.J., Pazyra-Murphy,M.F., Elliott,H.L. and Segal,R.A. (2016) The RNA-binding protein SFPQ orchestrates an RNA regulon to promote axon viability. *Nat. Neurosci.*, **19**, 690–696.
8. Takeuchi,A., Iida,K., Tsubota,T., Hosokawa,M., Denawa,M., Brown,J.B., Ninomiya,K., Ito,M., Kimura,H., Abe,T. *et al.* (2018) Loss of sfpq causes long-gene transcriptopathy in the brain. *Cell Rep.*, **23**, 1326–1341.
9. Ke,Y.D., Dramiga,J., Schutz,U., Kril,J.J., Ittner,L.M., Schroder,H. and Gotz,J. (2012) Tau-mediated nuclear depletion and cytoplasmic accumulation of SFPQ in Alzheimer's and Pick's disease. *PLoS One*, **7**, e35678.
10. Lu,J., Shu,R. and Zhu,Y. (2018) Dysregulation and dislocation of SFPQ disturbed DNA organization in alzheimer's disease and frontotemporal dementia. *J. Alzheimers Dis.*, **61**, 1311–1321.
11. Luisier,R., Tyzack,G.E., Hall,C.E., Mitchell,J.S., Devine,H., Taha,D.M., Malik,B., Meyer,I., Greensmith,L., Newcombe,J. *et al.* (2018) Intron retention and nuclear loss of SFPQ are molecular hallmarks of ALS. *Nat. Commun.*, **9**, 2010.
12. Lee,M., Sadowska,A., Bekere,I., Ho,D., Gully,B.S., Lu,Y., Iyer,K.S., Trewhella,J., Fox,A.H. and Bond,C.S. (2015) The structure of human SFPQ reveals a coiled-coil mediated polymer essential for functional aggregation in gene regulation. *Nucleic Acids Res.*, **43**, 3826–3840.
13. Lee,M., Passon,D.M., Hennig,S., Fox,A.H. and Bond,C.S. (2011) Construct optimization for studying protein complexes: obtaining diffraction-quality crystals of the pseudosymmetric PSPC1-NONO heterodimer. *Acta Crystallogr.*, **67**, 981–987.
14. Zhao,Q., Khorasanizadeh,S., Miyoshi,Y., Lazar,M.A. and Rastinejad,F. (1998) Structural elements of an orphan nuclear receptor-DNA complex. *Mol. Cell*, **1**, 849–861.
15. Aragao,D., Aishima,J., Cherukuvada,H., Clarken,R., Clift,M., Cowieson,N.P., Ericsson,D.J., Gee,C.L., Macedo,S., Mudie,N. *et al.* (2018) MX2: a high-flux undulator microfocus beamline serving both the chemical and macromolecular crystallography communities at the Australian Synchrotron. *J. Synchrotron Radiat.*, **25**, 885–891.
16. Kabsch,W. (2010) Xds. *Acta Crystallogr.*, **66**, 125–132.
17. Evans,P.R. and Murshudov,G.N. (2013) How good are my data and what is the resolution? *Acta Crystallogr.*, **69**, 1204–1214.
18. McCoy,A.J., Grosse-Kunstleve,R.W., Adams,P.D., Winn,M.D., Storoni,L.C. and Read,R.J. (2007) Phaser crystallographic software. *J. Appl. Crystallogr.*, **40**, 658–674.

19. Winn,M.D., Ballard,C.C., Cowtan,K.D., Dodson,E.J., Emsley,P., Evans,P.R., Keegan,R.M., Krissinel,E.B., Leslie,A.G., McCoy,A. *et al.* (2011) Overview of the CCP4 suite and current developments. *Acta Crystallogr.*, **67**, 235–242.
20. Emsley,P., Lohkamp,B., Scott,W.G. and Cowtan,K. (2010) Features and development of Coot. *Acta Crystallogr.*, **66**, 486–501.
21. Bricogne,G., E.,Blanc., Brandl,M., Flensburg,C., Keller,P., Paciorek,W., Roversi,P., Sharff,A., Smart,O.S., Vonrhein,C. and Womack,T.O. (2017) BUSTER version 2.10.3. Cambridge, United Kingdom: Global Phasing Ltd.
22. Chen,V.B., Arendall,W.B. 3rd, Headd,J.J., Keedy,D.A., Immormino,R.M., Kapral,G.J., Murray,L.W., Richardson,J.S. and Richardson,D.C. (2010) MolProbity: all-atom structure validation for macromolecular crystallography. *Acta Crystallogr.*, **66**, 12–21.
23. Bajaj,M., Mamidyala,S.K., Zuegg,J., Begg,S.L., Ween,M.P., Luo,Z., Huang,J.X., McEwan,A.G., Kobe,B., Paton,J.C. *et al.* (2015) Discovery of novel pneumococcal surface antigen A (PsaA) inhibitors using a fragment-based drug design approach. *ACS Chem. Biol.*, **10**, 1511–1520.
24. Kirby,N.M., Mudie,S.T., Hawley,A.M., Cookson,D.J., Mertens,H.D.T., Cowieson,N. and Samardzic-Boban,V. (2013) A low-background-intensity focusing small-angle X-ray scattering undulator beamline. *J. Appl. Crystallogr.*, **46**, 1670–1680.
25. Whitten,A.E., Cai,S.Z. and Trewhella,J. (2008) MULCh: modules for the analysis of small-angle neutron contrast variation data from biomolecular assemblies. *J. Appl. Crystallogr.*, **41**, 222–226.
26. Konarev,P.V., Volkov,V.V., Sokolova,A.V., Koch,M.H.J. and Svergun,D.I. (2003) PRIMUS: a Windows PC-based system for small-angle scattering data analysis. *J. Appl. Crystallogr.*, **36**, 1277–1282.
27. Svergun,D.I. (1992) Determination of the regularization parameter in indirect-transform methods using perceptual criteria. *J. Appl. Crystallogr.*, **25**, 495–503.
28. Svergun,D., Barberato,C. and Koch,M.H.J. (1995) CRYSOL - a program to evaluate x-ray solution scattering of biological macromolecules from atomic coordinates. *J. Appl. Crystallogr.*, **28**, 768–773.
29. Widagdo,J., Chai,Y.J., Ridder,M.C., Chau,Y.Q., Johnson,R.C., Sah,P., Huganir,R.L. and Anggono,V. (2015) Activity-dependent ubiquitination of GluA1 and GluA2 regulates AMPA receptor intracellular sorting and degradation. *Cell Rep.*, **10**, 783–795.
30. Tan,M.C., Widagdo,J., Chau,Y.Q., Zhu,T., Wong,J.J., Cheung,A. and Anggono,V. (2017) The activity-induced long non-coding RNA Meg3 modulates AMPA receptor surface expression in primary cortical neurons. *Front. Cell Neurosci.*, **11**, 124.
31. Hewage,T.W., Caria,S. and Lee,M. (2019) A new crystal structure and small-angle X-ray scattering analysis of the homodimer of human SFPQ. *Acta Crystallogr. F Struct. Biol. Commun.*, **75**, 439–449.
32. Huang,J., Casas Garcia,G.P., Perugini,M.A., Fox,A.H., Bond,C.S. and Lee,M. (2018) Crystal structure of a SFPQ/PSPC1 heterodimer provides insights into preferential heterodimerization of human DBHS family proteins. *J. Biol. Chem.*, **293**, 6593–6602.
33. Religa,D., Strozyk,D., Cherny,R.A., Volitakis,I., Haroutunian,V., Winblad,B., Naslund,J. and Bush,A.I. (2006) Elevated cortical zinc in Alzheimer disease. *Neurology*, **67**, 69–75.
34. Sensi,S.L., Rapposelli,I.G., Frazzini,V. and Mascetra,N. (2008) Altered oxidant-mediated intraneuronal zinc mobilization in a triple transgenic mouse model of Alzheimer's disease. *Exp. Gerontol.*, **43**, 488–492.
35. Dang,T.N., Lim,N.K., Grubman,A., Li,Q.X., Volitakis,I., White,A.R. and Crouch,P.J. (2014) Increased metal content in the TDP-43(A315T) transgenic mouse model of frontotemporal lobar degeneration and amyotrophic lateral sclerosis. *Front. Aging Neurosci.*, **6**, 15.
36. Kim,J., Kim,T.Y., Hwang,J.J., Lee,J.Y., Shin,J.H., Gwag,B.J. and Koh,J.Y. (2009) Accumulation of labile zinc in neurons and astrocytes in the spinal cords of G93A SOD-1 transgenic mice. *Neurobiol. Dis.*, **34**, 221–229.
37. Caragounis,A., Price,K.A., Soon,C.P., Filiz,G., Masters,C.L., Li,Q.X., Crouch,P.J. and White,A.R. (2010) Zinc induces depletion and aggregation of endogenous TDP-43. *Free Radic. Biol. Med.*, **48**, 1152–1161.
38. Frederickson,C.J., Koh,J.Y. and Bush,A.I. (2005) The neurobiology of zinc in health and disease. *Nat. Rev. Neurosci.*, **6**, 449–462.
39. Watt,N.T., Whitehouse,I.J. and Hooper,N.M. (2010) The role of zinc in Alzheimer's disease. *Int. J. Alzheimers Dis.*, **2011**, 971021.
40. Thomas-Jinu,S., Gordon,P.M., Fielding,T., Taylor,R., Smith,B.N., Snowden,V., Blanc,E., Vance,C., Topp,S., Wong,C.H. *et al.* (2017) Non-nuclear pool of splicing factor SFPQ regulates axonal transcripts required for normal motor development. *Neuron*, **94**, 322–336.
41. Szewczyk,B. (2013) Zinc homeostasis and neurodegenerative disorders. *Front. Aging Neurosci.*, **5**, 33.
42. McCord,M.C. and Aizenman,E. (2014) The role of intracellular zinc release in aging, oxidative stress, and Alzheimer's disease. *Front. Aging Neurosci.*, **6**, 77.
43. Leal,S.S., Botelho,H.M. and Gomes,C.M. (2012) Metal ions as modulators of protein conformation and misfolding in neurodegeneration. *Coordin. Chem. Rev.*, **256**, 2253–2270.
44. Sirangelo,I. and Iannuzzi,C. (2017) The role of metal binding in the amyotrophic lateral sclerosis-related aggregation of copper-zinc superoxide dismutase. *Molecules*, **22**, 1429.
45. Garnier,C., Devred,F., Byrne,D., Puppo,R., Roman,A.Y., Malesinski,S., Golovin,A.V., Lebrun,R., Ninkina,N.N. and Tsvetkov,P.O. (2017) Zinc binding to RNA recognition motif of TDP-43 induces the formation of amyloid-like aggregates. *Sci. Rep.*, **7**, 6812.
46. Dobson,L., Nyitray,L. and Gaspari,Z. (2015) A conserved charged single alpha-helix with a putative steric role in paraspeckle formation. *RNA*, **21**, 2023–2029.
47. Afroz,T., Hock,E.M., Ernst,P., Foglieni,C., Jambeau,M., Gilhespy,L.A.B., Laferriere,F., Maniecka,Z., Pluckthun,A., Mittl,P. *et al.* (2017) Functional and dynamic polymerization of the ALS-linked protein TDP-43 antagonizes its pathologic aggregation. *Nat. Commun.*, **8**, 45.
48. Ishigaki,S., Fujioka,Y., Okada,Y., Riku,Y., Udagawa,T., Honda,D., Yokoi,S., Endo,K., Ikenaka,K., Takagi,S. *et al.* (2017) Altered tau isoform ratio caused by loss of FUS and SFPQ function leads to FTLD-like phenotypes. *Cell Rep.*, **18**, 1118–1131.
49. Hergesheimer,R.C., Chami,A.A., de Assis,D.R., Vourc'h,P., Andres,C.R., Corcia,P., Lanznaster,D. and Blasco,H. (2019) The debated toxic role of aggregated TDP-43 in amyotrophic lateral sclerosis: a resolution in sight? *Brain*, **142**, 1176–1194.